Q. J. R. Meteorol. Soc. (1996), **122**, pp. 535–561

Dynamical structure functions in a four-dimensional variational assimilation: A case study

By JEAN-NOËL THÉPAUT,* PHILIPPE COURTIER, GILLES BELAUD and GWENDAL LEMAÎTRE
European Centre for Medium-Range Weather Forecasts, UK

(Received 7 March 1995; revised 21 August 1995)

SUMMARY

This paper contributes to the understanding of the structure functions used implicitly in the four-dimensional variational assimilation (4D-Var) developed at the European Centre for Medium-Range Weather Forecasts in the last few years. The theoretical equivalence between 4D-Var and the Kalman filter allows us to interpret (after normalization by the error standard deviations) the analysis increments produced by one single observation as the structure functions used implicitly in 4D-Var. The shape of the analysis increments provides a three-dimensional picture of the covariances of the background errors, modified by the dynamics.

We study a baroclinic situation and observations have been regularly distributed along a latitude circle crossing the baroclinic wave. Eight standard pressure levels have been considered to sample the vertical.

The forecast error standard deviations and the structure functions implied in 4D-Var may differ considerably from those used in the 3D-Var analysis. Unlike 3D-Var, the structure functions are flow dependent: the effective background error standard deviation can be four times larger and the correlation length scale twice as short in the vicinity of a low. A meridional extension of the experimentation at the surface shows that the effective background error standard deviations at 1000 hPa are largest in the areas of strong pressure gradient.

We quantify the link between the analysis increments produced by 4D-Var and the fastest growing perturbations over the same time interval. In the depression, the explained variance of the analysis increments by the first 13 singular vectors reaches 30%.

The impact of the temporal dimension is assessed. A period of 24 hours seems a minimum for the increments to develop fully baroclinic structures.

KEYWORDS: Kalman filter Singular vectors Structure functions Variational assimilation

1. INTRODUCTION

The potential of the 4D-Var data assimilation algorithm has been demonstrated for several years, first with simple models (Le Dimet and Talagrand 1986; Derber 1987; Talagrand and Courtier 1987; Courtier and Talagrand 1987; Courtier and Talagrand 1990) and more recently with 3-dimensional primitive equation models (see e.g. Thépaut and Courtier 1991; Navon *et al.* 1992; Rabier and Courtier 1992; Thépaut *et al.* 1993a).

4D-Var is able to extract information from the observations in a consistent way with the dynamics of the model. It also provides an elegant way of assimilating remotely sensed data, such as TOVS radiances (Andersson *et al.* 1994) or ERS-1 scatterometer backscatter coefficients (Thépaut *et al.* 1993b). Assuming the model is perfect, 4D-Var is equivalent to the fixed lag Kalman smoother (Ghil and Malanotte-Rizzoli 1991) (or to the Kalman filter for the result at final time); it uses flow-dependent structure functions, although it does not evolve them in time explicitly.

A practical way of exhibiting the implicit 4D-Var structure functions is to perform a 4D-Var assimilation with a single observation: the analysis increments are proportional to the forecast error covariances between the observed variable at the observation point and all other locations and variables.

Thépaut *et al.* (1993b) have shown how complex forecast error covariances can be when they evolve according to primitive equation dynamics, confirming results obtained in 2-D models using a Kalman filter by Cohn and Parrish (1991), and Gauthier *et al.* (1993). Following the methodology of Thépaut *et al.* (1993b), this paper presents a study of the structure functions implied in 4D-Var on a real meteorological situation with a baroclinic development in the Pacific Ocean.

* Corresponding author, current affiliation : Centre National de Recherches Météorologiques, Météo-France, Toulouse, France.

We first briefly summarize the 4D-Var formulation, its link with Kalman filtering and the differences between 3D-Var and 4D-Var (section 2). We then (in section 3) describe the experimental framework, the meteorological situation and the cost functions involved in 3D-Var and 4D-Var with a single observation. The spatial structure of the background error covariance model used in 3D-Var is documented in section 4. In section 5, the flow dependent structure functions used implicitly in 4D-Var are first presented for different observation locations. We then focus particularly on their shape close to a frontal system. The link between the 4D-Var increments and the unstable modes over the same time period is quantified. We lastly present the impact of the temporal dimension on the flow dependency of the forecast errors implied in 4D-Var. The notations follow Ide *et al.* (1995).

2. The 4D-Var problem

4D-Var finds a model solution which best fits observations available over a given period of time $[t_0, t_n]$ and background information available at t_0. Following Lorenc (1986) (and references in the introduction), one finds $\mathbf{x}^a = \mathbf{x}^a(t_0)$ (model state at the initial time t_0) which minimizes :

$$J(\mathbf{x}^a) = \frac{1}{2}(\mathbf{x}^a - \mathbf{x}^b)^T\mathbf{B}^{-1}(\mathbf{x}^a - \mathbf{x}^b) + \frac{1}{2}(\mathbf{H}\mathbf{x}^a - \mathbf{y})^T\mathbf{R}^{-1}(\mathbf{H}\mathbf{x}^a - \mathbf{y}). \quad (1)$$

Here $\mathbf{y}$ stands for the vector of observations (distributed in time and space), $\mathbf{x}^b$ for the background, $\mathbf{H}$ for the operator which predicts the observations from the model initial state, $\mathbf{R}$ for the covariance matrix of observation errors and $\mathbf{B}$ for the covariance matrix of background errors, ^{T} denotes the transpose. (1) is also the cost function for 3D-Var when $\mathbf{H}$ reduces to the calculation of the observed variables at the observation location. In 4D-Var $\mathbf{H}$ may also include the forecast model.

If the operator $\mathbf{H}$ (including the forecast) is linear, if the forecast error covariance used to initialize the Kalman filter at time t_0 is equal to the background error covariance $\mathbf{B}$ and if the forecast model is perfect, then the solution of 4D-Var and of the Kalman filter are equivalent (Daley 1991; Lorenc 1986 and Jazwinski 1970) in that they produce the same final estimate at time t_n. Furthermore, under the same conditions, 4D-Var produces the same solution over time $[t_0, t_n]$ as the Kalman smoother and, as a consequence, 4D-Var makes implicit use of flow-dependent forecast error covariances.

The geostrophic equilibrium imposed in $\mathbf{B}$ (Parrish and Derber 1992) ensures that the analysis increments are almost tangent to the Rossby manifold. In order to force the analysis (3D-Var or 4D-Var) to be very close to a nonlinear balance, a further term is added in practice to the cost function (1) which measures the distance to the slow manifold (Courtier and Talagrand 1990). This additional term has been found necessary in 3D-Var to obtain an analysis in nonlinear balance and to ensure that the subsequent evolution of surface pressure is free of spurious gravity wave oscillations (Courtier *et al.* 1993). Following Ghil *et al.* (1980), who addressed the point in the linear context, this may be interpreted as ensuring (in the equivalent Kalman filter) that the forecast error covariance matrix describes errors lying on the linear manifold tangent to the slow manifold. All the 4D-Var and 3D-Var experiments presented below contain such a gravity wave control term. We exclude it from the forthcoming algebraic development for the sake of simplicity of the presentation.

As discussed in Thépaut *et al.* (1993b), the equivalence of 4D-Var and the Kalman filter is only approximate, since the forecast model is not linear. However, over 24 hours the evolution of perturbations of magnitude comparable to the background errors is governed

to a good approximation by the tangent linear model. The observation operator is almost linear in the following experiments where only height observations are used. The forecast model is not perfect either, however we will see that the main results obtained are related to large scale baroclinic instability which is represented in the model and whose evolution is fairly well described by the tangent linear model (Rabier and Courtier 1992).

In an analysis (3D-Var or OI or at each analysis step of a Kalman filter), the analysis increments, $\mathbf{x}^a - \mathbf{x}^b$, are a linear combination of the observation increments, $\mathbf{y} - \mathbf{H}\mathbf{x}^b$, (Lorenc 1986, Eq. (28)),

$$\mathbf{x}^a - \mathbf{x}^b = \mathbf{B}\mathbf{H}'^{\mathrm{T}}(\mathbf{H}'\mathbf{B}\mathbf{H}'^{\mathrm{T}} + \mathbf{R})^{-1}[\mathbf{y} - \mathbf{H}\mathbf{x}^b] \tag{2}$$

where $\mathbf{H}'$ is the linearization of $\mathbf{H}$ in the vicinity of the background $\mathbf{x}^b$. Considering one single observation, $\mathbf{H}'^{\mathrm{T}}$ becomes a vector of the same dimension as the model state vector which will be denoted by $\mathbf{h}^{\mathrm{T}}$; (2) reduces to

$$\mathbf{x}^a - \mathbf{x}^b = \mathbf{B}\mathbf{h}^{\mathrm{T}}\left(\frac{\mathbf{y} - \mathbf{H}\mathbf{x}^b}{\sigma_b^2 + \sigma_o^2}\right) \tag{3}$$

where σ_b^2 is the implicitly specified error variance of the background equivalent to the observation ($\sigma_b^2 = \mathbf{h}\mathbf{B}\mathbf{h}^{\mathrm{T}}$), σ_o^2 is the observation error variance and $\mathbf{B}\mathbf{h}^{\mathrm{T}}$ is the background error covariance of all the model variables with the model equivalent to the observation: the analysis increments are proportional to the background error covariance of all the model variables with the background equivalent to the observation. This also holds for 4D-Var: with a single observation at time t_n, the observation operator $\mathbf{H}$ is equivalent to a transport from time t_0 to time t_n with the tangent linear model $\mathbf{M}'$ and then, followed by the application of h, (2) becomes (for an observation at time t_n):

$$\mathbf{x}^a(t_0) - \mathbf{x}^b(t_0) = \mathbf{B}\mathbf{M}'^{\mathrm{T}}\mathbf{h}^{\mathrm{T}}\left(\frac{\mathbf{y} - \mathbf{H}\mathbf{x}^b(t_n)}{\sigma_b^2 + \sigma_o^2}\right) \tag{4}$$

with

$$\sigma_b^2 = \mathbf{h}\mathbf{M}'\mathbf{B}\mathbf{M}'^{\mathrm{T}}\mathbf{h}^{\mathrm{T}} \tag{5}$$

The analysis increments may be considered at time t_n (assuming implicitly an accurate tangent linear dynamics)

$$\mathbf{x}^a(t_n) - \mathbf{x}^b(t_n) = \mathbf{M}'(\mathbf{x}^a(t_0) - \mathbf{x}^b(t_0)) = \mathbf{M}'\mathbf{B}\mathbf{M}'^{\mathrm{T}}\mathbf{h}^{\mathrm{T}}\left(\frac{\mathbf{y} - \mathbf{H}\mathbf{x}^b(t_n)}{\sigma_b^2 + \sigma_o^2}\right). \tag{6}$$

In 4D-Var, using a single observation, the analysis increments are proportional to $\mathbf{M}'\mathbf{B}\mathbf{M}'^{\mathrm{T}}\mathbf{h}^{\mathrm{T}}$ which may be interpreted as the background error covariance of all model variables with the model equivalent to the observation at time t_n. The expression is equivalent to the term used in the analysis step at time t_n of a Kalman filter, since (6) may be obtained from (3) by replacing $\mathbf{B}$ with $\mathbf{M}'\mathbf{B}\mathbf{M}'^{\mathrm{T}}$.

Applying $\mathbf{h}$ to (6) one finds for the analysis increments at the observation point:

$$\mathbf{h}(\mathbf{x}^a(t_n) - \mathbf{x}^b(t_n)) = \mathbf{h}\mathbf{M}'\mathbf{B}\mathbf{M}'^{\mathrm{T}}\mathbf{h}^{\mathrm{T}}\left(\frac{\mathbf{y} - \mathbf{H}\mathbf{x}^b(t_n)}{\sigma_b^2 + \sigma_o^2}\right) = \left(\frac{\sigma_b^2}{\sigma_b^2 + \sigma_o^2}\right)(\mathbf{y} - \mathbf{H}\mathbf{x}^b(t_n)). \tag{7}$$

One also notices that to first order,

$$\mathbf{h}(\mathbf{x}^a(t_n) - \mathbf{x}^b(t_n)) = \mathbf{H}\mathbf{x}^a(t_n) - \mathbf{H}\mathbf{x}^b(t_n) \tag{8}$$

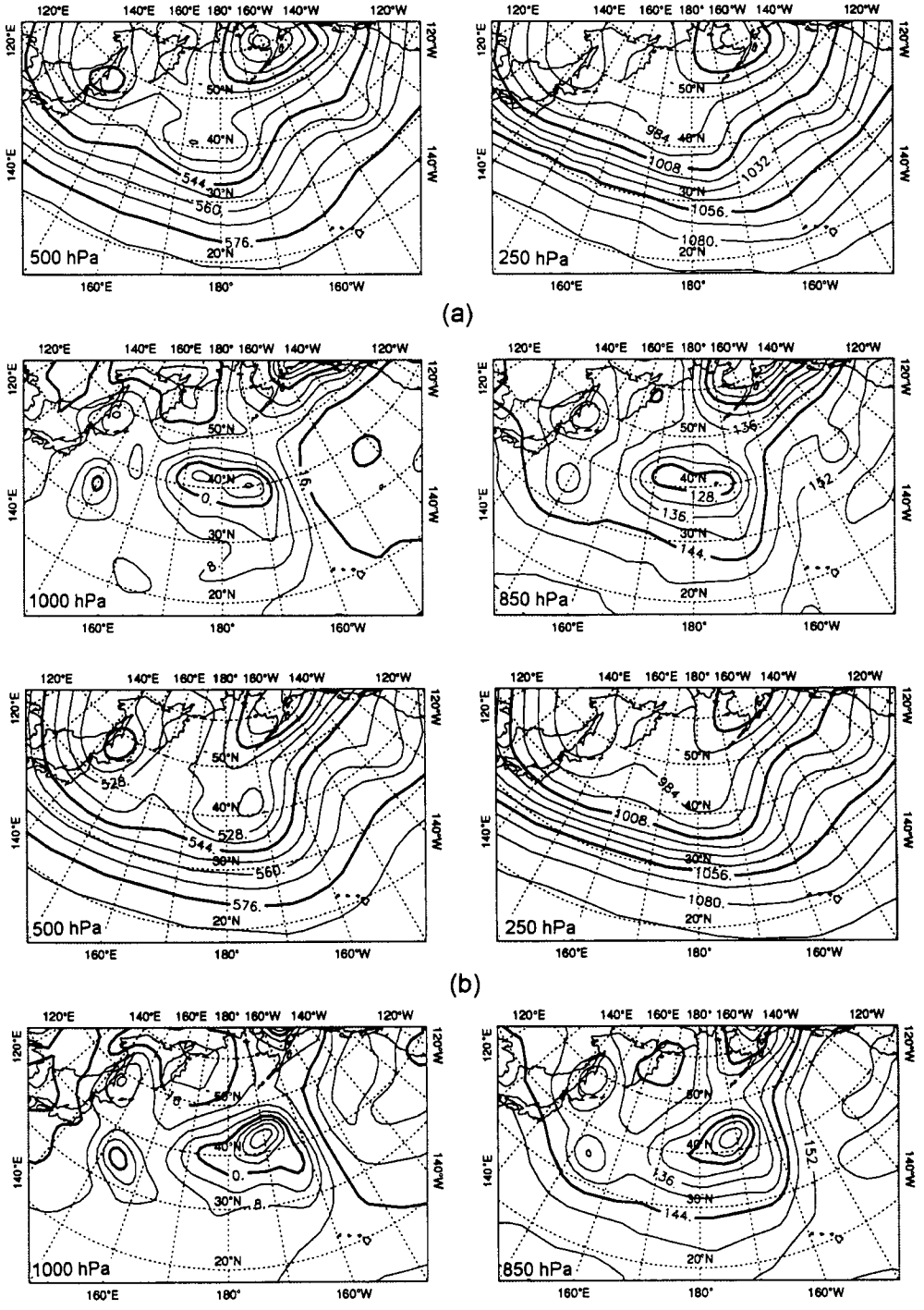

Figure 1. Background fields for 1200 UTC 4 March 1994 (a), 0000 UTC 05 March 1994 (b), 1200 UTC 5 March 1994 (c). Shown here are the Pacific Ocean 250 hPa, 500 hPa, 850 hPa and 1000 hPa geopotential height fields. The fields for 4 March are from the initial estimate of the initial conditions for the 4D-Var minimization. The fields for 5 March 0000 UTC (1200 UTC) are from the 12-hour (24-hour) T63 adiabatic model forecast from the initial conditions. (d) is the satellite image, superimposed with the geopotential height field for 1200 UTC 5 March 1994. Contour intervals : 40 m.

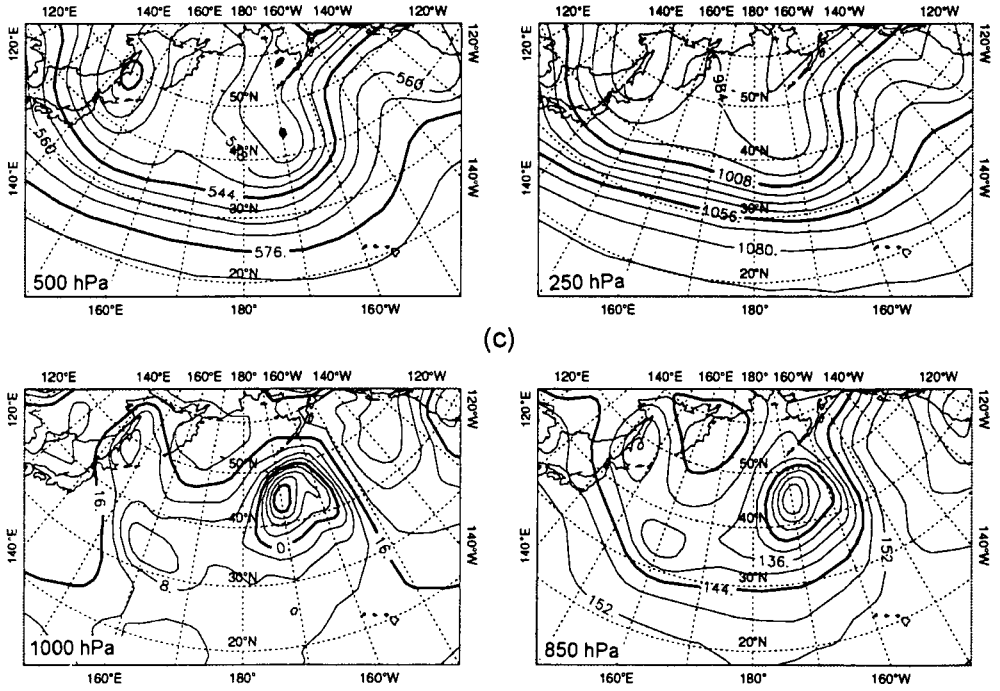

Figure 1. Continued.

from which we find:

$$\sigma_b^2 = \sigma_o^2 \left(\frac{\mathbf{H}\mathbf{x}^a(t_n) - \mathbf{H}\mathbf{x}^b(t_n)}{\mathbf{y} - \mathbf{H}\mathbf{x}^a(t_n)} \right) \tag{9}$$

An algorithm is provided by (9) in 4D-Var (but also in 3D-Var) to compute at time t_n the effective background error variance of the model equivalent to a particular observation.

Remark 1: All the above discussion is strictly valid in the linear case. It generalizes to the quasi-linear context (within the range of validity of the tangent linear approximation).

Remark 2: (6) may be multiplied by any linear operator e.g. a postprocessing. The result can be interpreted as the covariances of the background errors of the postprocessed model variables with the model equivalent to the observation.

In the following, for the specified observation we will use a standard pressure level height measurement and the model variables will be postprocessed to standard pressure level heights. This will allow us to explicitly determine the height-height covariance matrix of background error which is implicit in the variational assimilation. We have chosen to work with height because of the vast experience acquired in its operational use in Optimal Interpolation (Lönnberg and Hollingsworth 1986).

Remark 3: If one would be interested in depicting the covariances of the analysis errors (and not of the background errors as in this study), a similar methodology may be applied. One has to compare the two analyses obtained first with all the observations and then with all the observations plus a synthetic observation.

The 3D-Var non-separable structure functions (Courtier *et al.* 1993) will be briefly compared with optimal interpolation for the sake of validation and illustration of the methodology. We shall then concentrate on the 4D-Var flow dependent structure functions.

3. Experimental framework

(*a*) *The meteorological situation*

For this study we have chosen an unexceptional situation presenting the deepening and displacement of a low over the Pacific Ocean.

Figure 1(a) presents the background geopotential height field for 3 April 1994 1200 UTC, obtained from the European Centre for Medium-Range Weather Forecasts (ECMWF) T213L31 operational analysis, interpolated at T63L19 resolution and initialized with non-linear normal mode initialization. The fields at 3 May 1994 0000 UTC and 3 May 1994 1200 UTC are depicted on Fig. 1(b) and 1(c) and have been produced from a 12- and 24-hour forecast respectively with a T63L19 nearly adiabatic version of the IFS model (Courtier *et al.* 1991). Horizontal diffusion, a simplified surface friction and vertical diffusion are included. The 24-hour adiabatic evolution remains similar to the full model evolution (not shown) and to the real situation (Fig. 1(d)), even if in reality the low has moved faster as can be seen from the satellite imagery.

At 1200 UTC on 4 March, a depression in the 1000 hPa height field has two centres at 175°E and 175°W close to 40°N. At 500 hPa, a large trough is centred at 175°E presenting an extension to the west up to 165°E almost leading to a cut off. A ridge is located at 160°E.

Twelve hours later, the depression at the surface has moved 3 degrees N and 3 degrees E and has deepened by 40 m (around 5 hPa). At 500 hPa, the trough has also intensified and the ridge on its eastern side has moved 10 degrees eastward and strengthened.

After 24 hours, the depression has deepened by a further 40 m. East of the occlusion, a sharp front is present at 160°W; the occlusion remains stationary between 0000 and 1200

UTC its progress being blocked by the anticyclone strengthening at (140°W, 45°N). At 500 hPa, the trough has deepened further and is now located at 40°N-170°W. The eastern ridge has also intensified and has moved by 20 degrees in 24 hours. West of the trough, the ridge has moved 10 degrees eastward.

(*b*) *Assimilation experiments*

Our estimation of the structure functions is made through a series of 3D-Var or 4D-Var analyses, each analysis using a single observation. The observations have been first specified at different points on latitude 42°N, thus crossing the low and the anticyclone, from longitude 157.5°E to 142.5°W. (This parallel is the 26th of the T63 Gaussian grid). The position of the observations changes by 7.5 degrees in longitude between successive analyses in the series and the sampling density was increased by a factor of 4 in crucial areas like the depression. They are vertically located at standard pressure levels from 1000 hPa to 200 hPa. The synthetic observation value is obtained by adding one metre to the height background value.

An observational departure of one metre has been chosen to ensure that the 24-hour evolution of the associated errors is well described by the tangent linear model (which is the basic hypothesis for interpreting the analysis increments as covariances), while also keeping a good degree of accuracy when computing the analysis increments from differences between the background and the analysis of archived (and packed) fields.

For the minimization, we rely on the M1QN3 package provided by INRIA (Gilbert and Lemarechal 1989). Between 22 and 30 iterations have been found sufficient in 4D-Var to obtain an accuracy of 1% for the implied error standard deviation. Due to the uncertainty arising from the approximate convergence and from the remaining non-linearities associated to the finite amplitude perturbation, a lack of symmetry of almost 2% in the correlation matrices was noticed, this lack of symmetry being less than 1% most of the time. We will then consider correlation differences larger than 10 % as significant.

4. Structure functions in 3D-Var

(*a*) *Spatial aspects*

The (Z–Z) correlations specified in the ECMWF OI are homogeneous and isotropic on the f-plane (Shaw *et al.* 1987; Undén 1989; and references therein). The multivariate formulation follows Daley (1991). In OI, for computational convenience, the assumption is usually made that correlations are a separable function of pressure and horizontal separation (Lönnberg and Hollingsworth 1986). In 3D-Var, it is more convenient to express them in spectral/normal mode space (Phillips 1986). This has the advantage of allowing a non-separable statistical model: the vertical background error covariance matrix varies with the total wave number. Apart from this feature the (Z–Z) model of OI and 3D-Var are very similar in the troposphere (Courtier *et al.* 1993) while in the stratosphere they differ because of an increased horizontal length scale in 3D-Var.

Figure 2 presents the geopotential height increments for an observation at 850 hPa. They have a circular shape which is in agreement with the isotropic (Z–Z) covariances (constant horizontal background error standard deviations for vorticity and height are used in this experiment). The divergence increment is two orders of magnitude smaller than the vorticity increments at this level, which is consistent with the geostrophy imposed in the background error covariances.

Vertical cross-sections of the height analysis increments (not shown) are also symmetric with respect to the vertical of the observation. The maximum amplitude of the

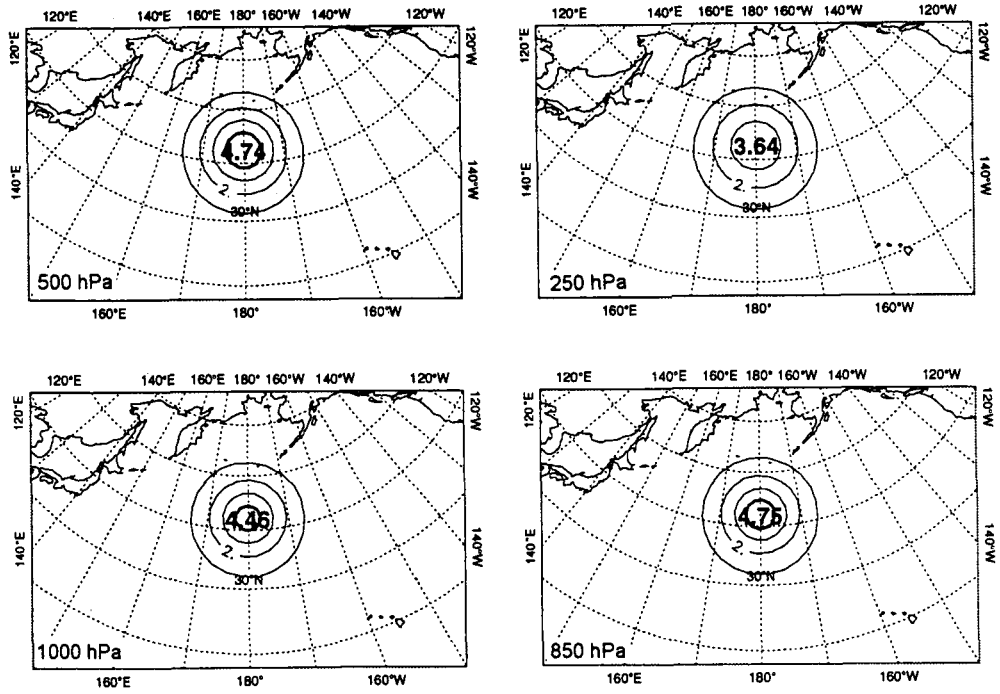

Figure 2. The 3D-Var analysis increments (analysis–background), at the end of the 24-hour assimilation period, for geopotential height and at 1000, 850, 500 and 250 hPa, corresponding to a single height observation at 500 hPa at the location (42°N, 180°E). Contour interval: 0.1 m.

TABLE 1. EFFECTIVE HEIGHT BACKGROUND ERROR STANDARD DEVIATIONS IN 3D-VAR AT 42°N

height (hPa)	σ_b (m)
1000	12.618
850	11.972
700	13.853
500	20.835
400	25.669
300	27.966
250	27.477
200	24.092

increments in the vertical is not necessarily attained at the observation level, since the variances of the background error depend on height. The values of the effective height background error standard deviations at the location (42°N, 180°E) calculated according to (9) and for the different pressure levels are in Table 1. In 3D-Var, the variances are constant (at a given latitude) along a model level, rather than along a pressure level as in the OI covariance model. In practice, the effective height error standard deviations varied horizontally by 8% at 1000 hPa whereas it varied by only 0.8% at level 250 hPa.

Using the proportionality of the analysis increments to the background error covariances (Eq. 6), we can deduce the background error correlation between the points i and j:

$$\mathrm{cor}(i, j) = \frac{\mathbf{H}\mathbf{x}_j^{\mathrm{a}}(t_n) - \mathbf{H}\mathbf{x}_j^{\mathrm{b}}(t_n)}{\mathbf{H}\mathbf{x}_i^{\mathrm{a}}(t_n) - \mathbf{H}\mathbf{x}_i^{\mathrm{b}}(t_n)} \cdot \frac{\sigma_{\mathrm{b}}(i)}{\sigma_{\mathrm{b}}(j)} \tag{10}$$

where $x_i^{\mathrm{a}}(t_n)$ is the analysis produced by the observation at point i.

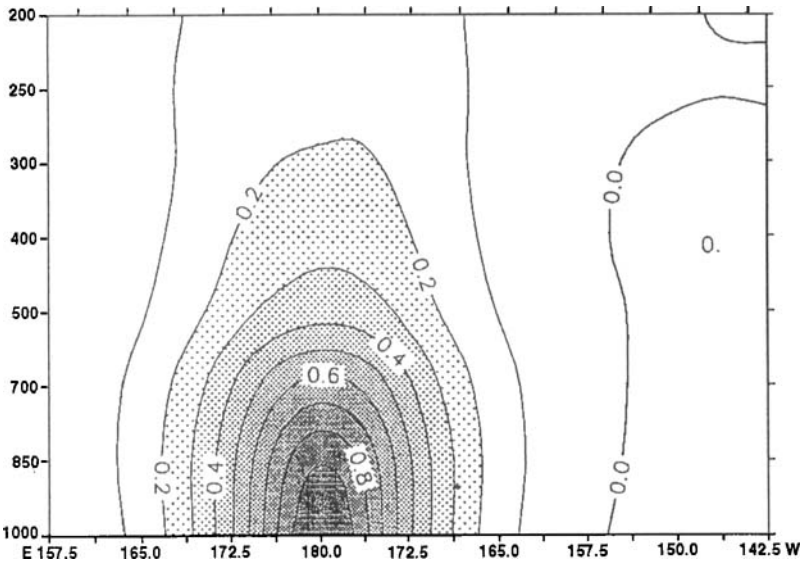

Figure 3. Cross-section of the 3D-Var structure function for an observation at location (42°N, 168.75°W, 1000 hPa). Contour interval: 0.1 m.

Figure 3 shows the cross-section of the correlations for an observation at 1000 hPa located at (42°N, 180°E). These results are consistent with the statistical model described in Courtier *et al.* (1993).

(*b*) *Spectral aspects*

The thin curves of Fig. 4 display the power spectra as a function of the total wave number m of the geopotential height increments for the three levels: 250 hPa, 500 hPa, 1000 hPa obtained with a single observation located respectively at the same levels 250 hPa, 500 hPa, 1000 hPa. We checked that the horizontal variation of the spectra with the geographical location of the observation is negligible. Denoting by Φ_n^m the spectral coefficient of the spherical harmonic expansion of the geopotential increments, their power spectrum is defined by:

$$e(m) = 2\sum_{n=1}^{m} \Phi_n^m \Phi_n^{m*} + \Phi_n^0 \Phi_n^{0*} \tag{11}$$

where * denotes the complex conjugate and the factor of two arises from the negative value of m. As said in section 2, the analysis increments are proportional to the effective covariance of forecast error which we denote by c:

$$\Phi_n^m = \alpha c_n^m. \tag{12}$$

The specified covariances for vorticity and for the ageostrophic part of the height are isotropic (Courtier *et al.* 1993). The effective geopotential covariances are then very close to isotropic for scales shorter than the Rossby radius of deformation. Consequently, in the following, we only consider in the isotropic part that we denote $c(m)$.

From (12) we have:

$$e(m) = \alpha^2 c(m)^2. \tag{13}$$

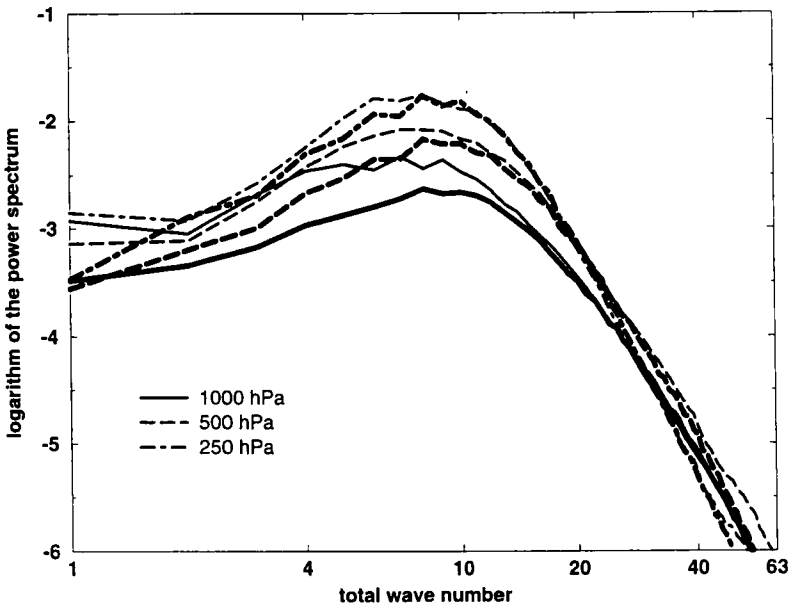

Figure 4. 3D-Var geopotential increments power spectrum logarithm as a function of the total wave number m and for an observation located at height 1000 (full), 500 (dashed) and 250 (dashed-dotted) hPa. In thick lines are represented the equivalent power spectra logarithm of the statistics entered in the background error covariance matrix of the 3D-Var system.

Rabier and Mc Nally (1993) computed the statistics of the isotropic part of the mass field ($P = \Phi + RT \ln(p_s)$) forecast error (denoted $\tilde{c}$) on hybrid coordinates. The thick line of Fig. 4 depicts $\tilde{c}^2$ multiplied by a proportionality factor such that the thick and thin curves are coincident at number wave 30.

In the inertial range the thick and thin curves of Fig. 4 agree almost perfectly, which may be considered as a validation of the 3D-Var formulation. However, the matching of the curves is not as good for the large scales. This lack of agreement may arise from two sources:

(i) If the vorticity error covariance is assumed to be isotropic, the geopotential errors become elongated in the east–west direction for the large scales (Daley 1991).

(ii) The assumption in 3D-Var that the geopotential errors are a function of the vorticity errors is probably not very accurate for scales larger than the Rossby radius of deformation.

5. Structure functions in 4D-Var

As discussed in section 2, 4D-Var implicitly evolves the background error covariances in time. As a consequence, and in contrast to static analysis schemes such as 3D-Var, 4D-Var is able to use flow-dependent structure functions. Section 2 also mentioned that the analysis increments from a single datum are proportional to the covariance of the background error. In 3D-Var it is $\mathbf{B}$ from (1) whereas in 4D-Var it becomes $\mathbf{M}'\mathbf{B}\mathbf{M}'^{\mathrm{T}}$.

In the 4D-Var experiments presented below, the background error covariance matrix used at t_0 is identical to the 3D-Var one. We have adopted the same experimental framework as in the previous section: a series of assimilations with single observations regularly spaced along the 42°N parallel and vertically located at standard pressure levels.

(*a*) *Spatial aspects*

(i) *Analysis increments.* Figures 5 to 7 depict the geopotential height increments at four levels (1000, 850, 500 and 250 hPa) produced by 4D-Var at the end of the assimilation period resulting from the use of a 850 hPa height observation located on latitude 42°N, respectively at 170.6°W, 168.75°W and 142.5°W.

The spatial propagation of the information within 4D-Var is significantly different from 3D-Var. The increments are anisotropic and are no longer symmetric with respect to the observation location. The homogeneity is also lost: the increments depend on the observation location

Close to the centre of the surface low (Fig. 5), the maximum of the 4D-Var increments (10 dm) is twice the 3D-Var value (Fig. 2). At 850 hPa, a second maximum of 4 dm located appears at 160°W, corresponding to the the warm sector of the weather system. There is also a negative extremum at the edge of the eastern ridge (160°W–50°N). At 1000 hPa, the increments are even larger than at 850 hPa (maximum of 12 dm) and one can again notice the connection between the occlusion and the warm sector. At 500 and 250 hPa, the increments are of broader scale, the positive (negative) ones follow the patterns of the trough (ridge) fairly closely, showing a global dynamical consistency of the increments with the meteorological situation.

Close to the low centre, the length scale of the increments is significantly different in 4D-Var compared to 3D-Var: they are halved in 300 km in 4D-Var along the 42°N parallel, compared to 600 km in 3D-Var (Fig. 2).

If the observation is moved 1.875 degrees to the east (Fig. 6), the increments are concentrated east of the occlusion, with a local maximum of 8.3 dm at the cold front.

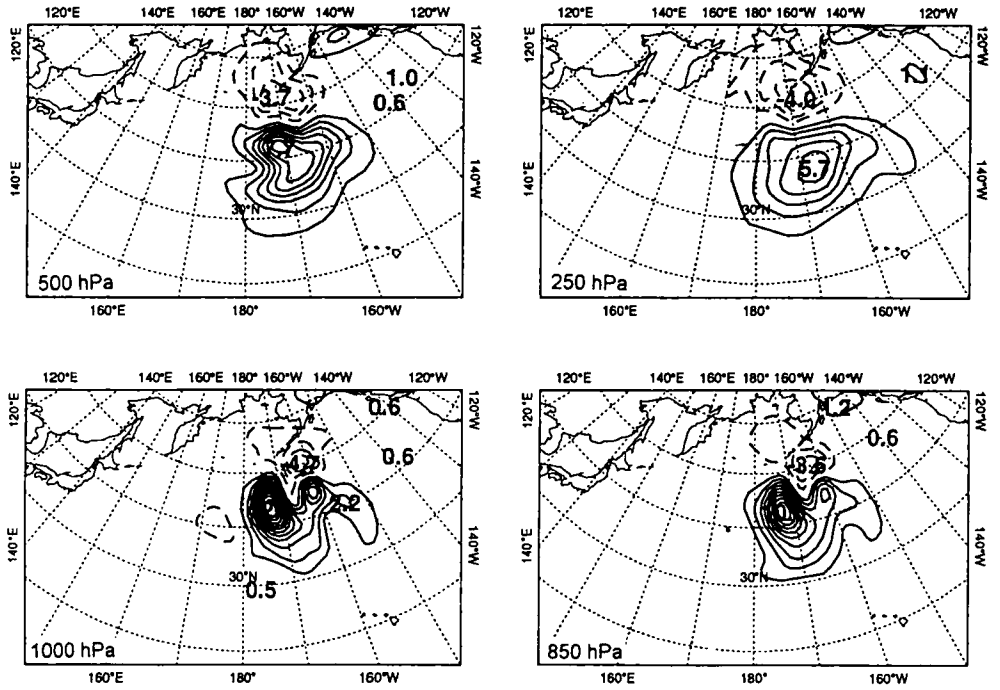

Figure 5. The 4D-Var analysis increments (analysis–background) for geopotential height and at 1000, 850, 500 and 250 hPa, corresponding to a single height observation at 850 hPa at the location (42°N, 170.625°W). Contour interval: 0.1 m.

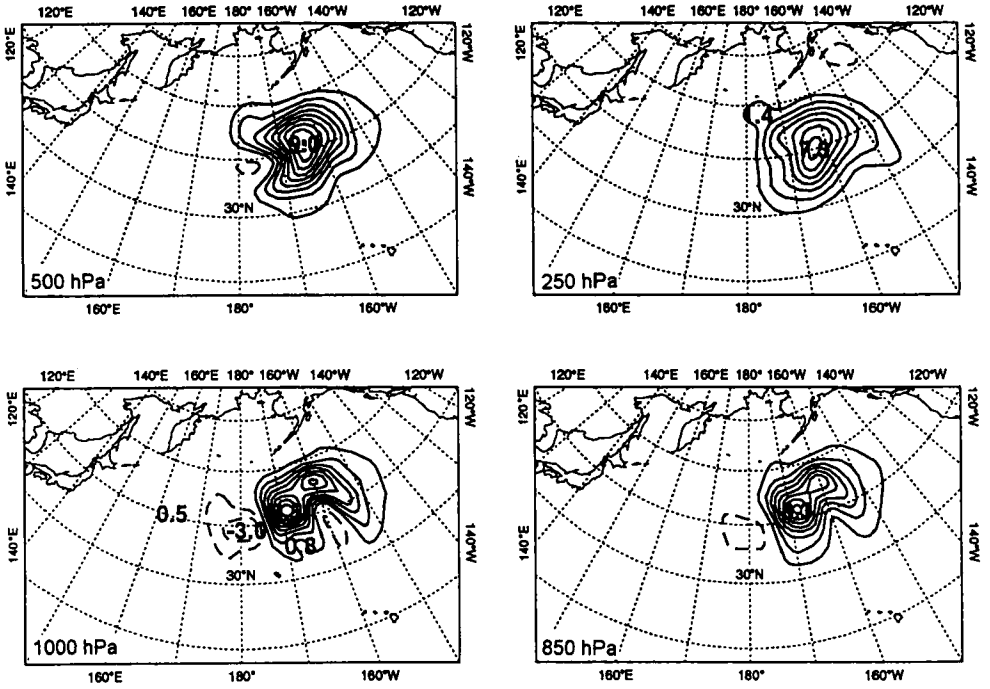

Figure 6. The 4D-Var analysis increments (analysis–background) for geopotential height and at 1000, 850, 500 and 250 hPa, corresponding to a single height observation at 850 hPa at the location (42°N, 168.75°W). Contour interval: 0.1 m.

There is also a negative increment behind the occlusion corresponding to a displacement of the atmospheric system from east to west.

To interpret these displacements, one can multiply by a factor of 100 the increments which would correspond to an observation departure of 100 m (roughly 12 hPa) and compare, for instance, the surface background and analysis height fields at latitude 42°N. Such an observation at location (42°N, 180°E, 1000 hPa) would then produce a deepening of the low of 5 hPa and a displacement of 200 km eastward. A symmetrical result is obtained with the same observation located east of the occlusion.

When the observation is located in the anticyclonic area (Fig. 7), the amplitude of the 4D-Var and 3D-Var increments is similar. The maximum is 4.5 dm at level 850 hPa as in 3D-Var (Fig. 2). For an observation located at 500 hPa the maximum increment is 9.4 dm in 4D-Var, compared to 8.7 dm in 3D-Var (not shown). However, the horizontal extension of the increments is wider. In the ridge, the increments at the observation level are halved in 1500 km from east to west along the parallel 42°N, which is five times larger than for the observation in the low. One can see on Fig. 7 that an observation located at 142.5°W produces positive increments up to (40°N, 170°W) and negative ones at location (50°N, 170°W), implying a northward shift of the low.

Figure 8 presents a cross-section along the parallel 42°N of the vorticity field at the end of the assimilation period, which illustrates the baroclinic structure of the atmospheric situation. Fig. 1 (panel c) shows that the section crosses the occluded part of the low at longitude 170°W, the positive vorticity values extending up to jet level. The section then crosses the cold front at longitude 155°W, the positive vorticity connecting at level 500 hPa with the occluded part.

Figure 9 presents the cross section of the height analysis increments for an observation

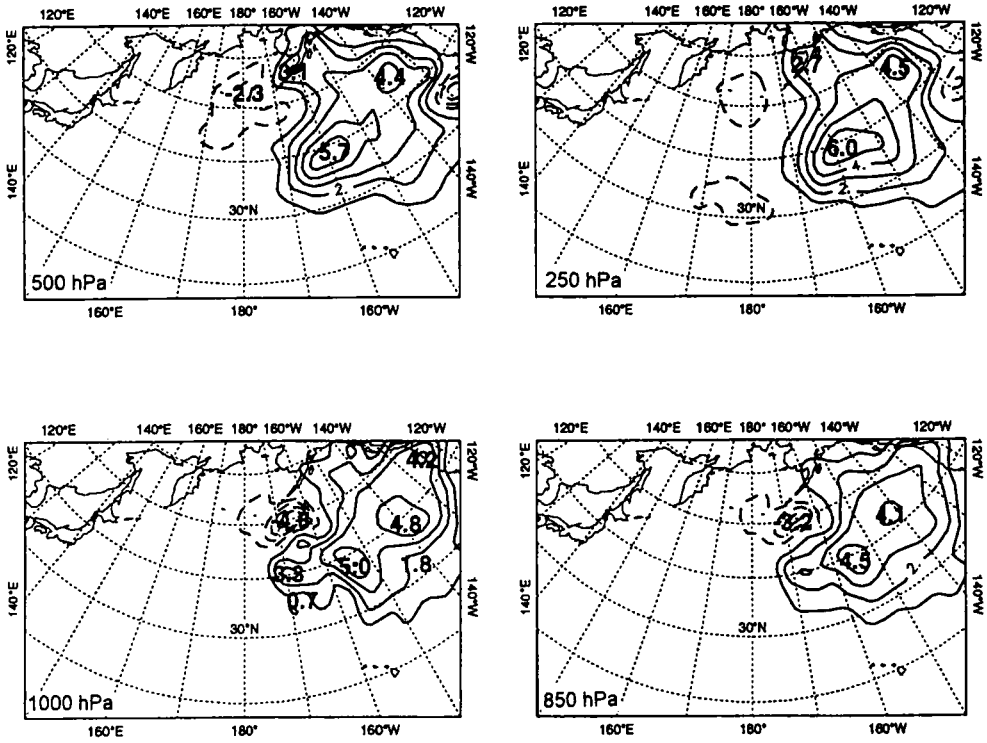

Figure 7. The 4D-Var analysis increments (analysis–background) for geopotential height and at 1000, 850, 500 and 250 hPa, corresponding to a single height observation at 850 hPa at the location (42°N, 142.5°W). Contour interval: 0.1 m.

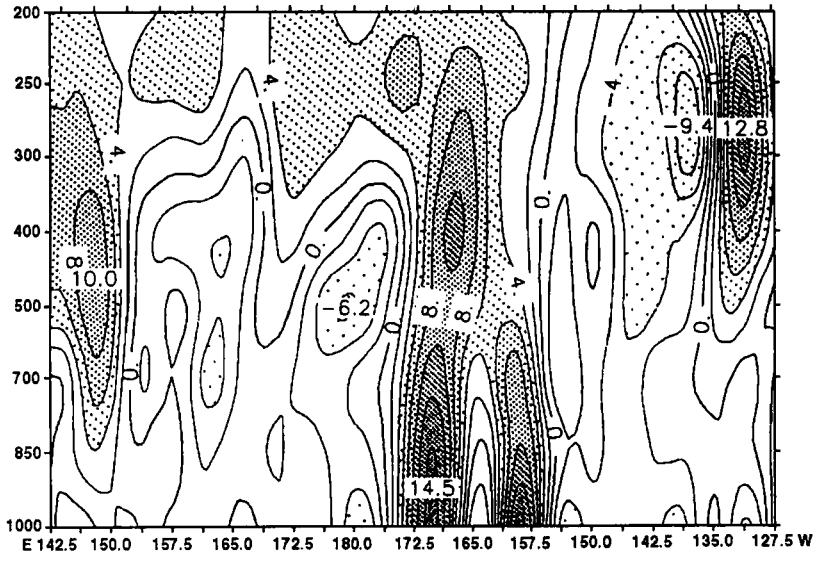

Figure 8. Vorticity field cross-section at latitude 42°N, multiplied by a factor 10^5. Contour interval: 2 s^{-1}.

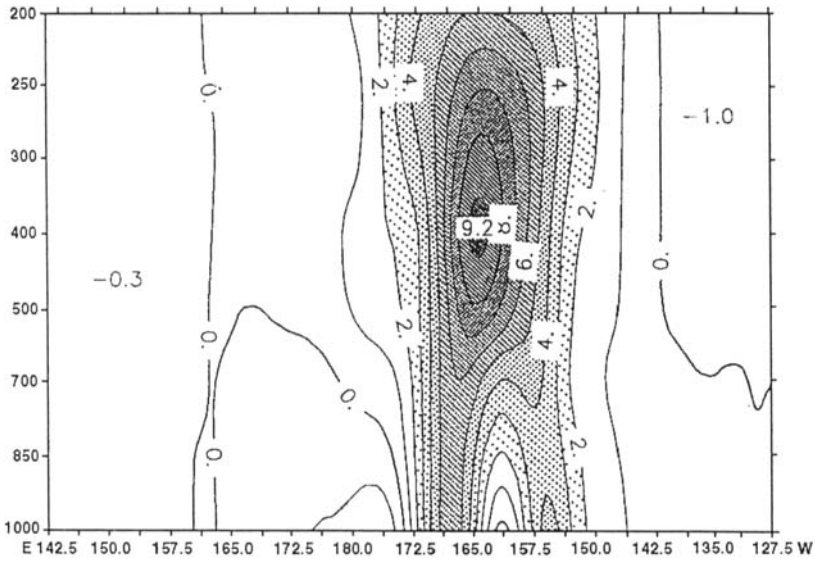

Figure 9. Cross-section of the 4D-Var analysis increments corresponding to an observation located at (42°N, 165°W) at 400 hPa. Contour interval: 0.1 m.

at location (42°N, 165°E), level 400 hPa. The baroclinic structure of these increments is remarkable. The shape of the two warm sectors at lower levels is present, one from longitude 170 to 165°W west of the cold front, the other one from longitude 157 to 150°W, east of the cold front. The connection between the two air masses is visible on both cross-sections, with a local maximum at around 400 hPa.

(ii) *Implied standard deviations*. To explore the flow dependency of the forecast error variances implicitly used in 4D-Var, we have computed, according to (9), the effective σ_bs at all the observation locations. Those σ_bs are, of course, no longer constant either vertically or horizontally, since the term $\mathbf{M}'\mathbf{B}(t_0)\mathbf{M}'^{\mathrm{T}}$ (see 5) is involved in the computations.

Figure 10 (panel a) shows the cross-section of the background error standard deviations in 4D-Var. The variances of the background error are maximum (reaching a value of 50 m) immediately west of the low at 1000 hPa where the surface pressure gradient is maximum according to Fig. 1 (panel c), and is minimum where the dynamics is stable with values similar as in 3D-Var. The patterns of the σ_b field match the perturbed system depicted in Fig. 8, in particular the maximum at 400 hPa and the unstable area east of the cold front.

Figure 10 (panel b) shows the cross-section of the σ_bs normalized by the 3D-Var values which are constant at a given level. This shows the spatial variability of the background error variances inferred by the dynamics used in 4D-Var (on top of the usual barotropic and isotropic 3D-Var structures) in the presence of unstable meteorological conditions. From longitude 180° to 157°W and in the lower troposphere below 700 hPa, the σ_bs are more than twice as high as in 3D-Var, except in the cold air at longitude 162°W. At the surface, we have a maximum ratio of four at longitude 174.375°W, west of the occlusion. The ratio is close to 1 at the jet level in the low. At levels 400 and 500 hPa and on the ridge (from 155°W to 142.5°W), the effective σ_bs are lower in 4D-Var, with a minimum ratio of 0.6.

Since the horizontal variation of the effective σ_bs was maximum at the surface, we have extended the computations at 1000 hPa in the latitude-longitude sector 180°/150°W–

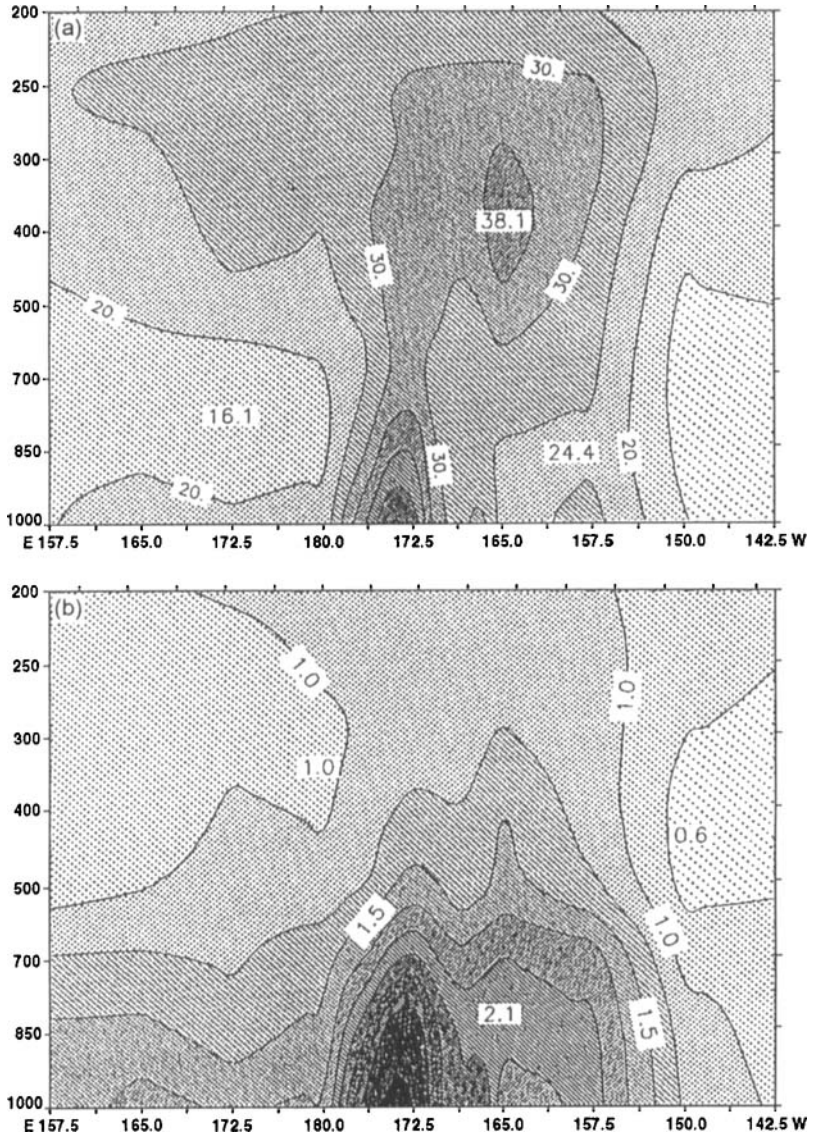

Figure 10. (a) Cross-section at latitude 42°N of the background error standard deviation in 4D-Var 24 hours. Contour interval : 5 m (b) Cross-section at latitude 42°N of ratio of the background error standard deviation in 4D-Var and 3D-Var. Contour interval: 0.25.

34.5°N/53.15°N. The 1000 hPa background height field and the effective σ_b field are superimposed in Fig. 11. High values of the σ_b field are clearly located along the areas of strong gradients of the background height field, with maxima colocated with the fronts.

This can be partially explained by a phase error in the advection: if one assumes the height field to evolve according to a linear advection equation, and furthermore that a phase error arises from an error in the advective wind field, then the amplitude of the background error variance will be maximum where the height gradient is maximum. This can easily be shown by deriving the equation describing the error variance evolution in a linear advection dynamics. No doubt, however, that more complex features related to baroclinic instability are responsible for the horizontal variation of the background error standard deviations.

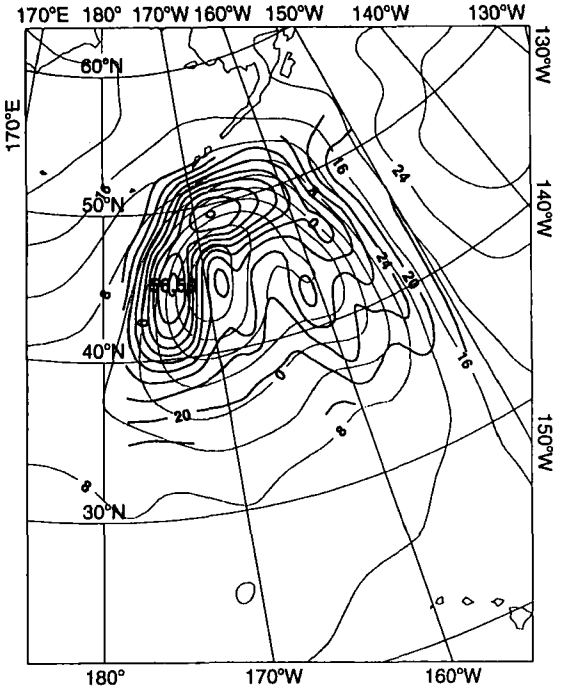

Figure 11. Field of effective σ_bs used in 4D-Var at the end of the assimilation at 1000 hPa. The field of σ_bs (thick) is superimposed on top of the 1000 hPa field (thin).

This demonstrates how inappropriate the static background error variance used in 3D-Var or OI can be in unstable areas.

(iii) *Implied structure functions.* Figure 12 shows a vertical cross-section of the 4D-Var error correlation field computed following (10) for an observation located at 1000 hPa in the warm sector of the low (42°N, 168.75°W). This figure is to be compared to the 3D-Var error correlation field (Fig. 3). The symmetry with respect to the vertical of the observation location is lost with a rapid decrease of the correlation on the eastern part of the occluded front and a negative value west of the occlusion. In the cold air, the correlation is very small: 0.2 at longitude 162°W, whereas 3D-Var would give a correlation of 0.5. The correlation rapidly increases in the warm sector, to reach 0.7 at 152°W whereas 3D-VAR leads to a correlation of 0.1 at this distance. Another remarkable feature is the vertical propagation of the error correlation. A correlation of near 1 extends up to 700 hPa. Up to 300 hPa, the correlation is 0.8 against 0.2 in 3D-Var.

(iv) *Link with the unstable modes.* One can compare the 4D-Var increments produced at the end of the assimilation period with the fastest growing perturbations computed over the same time interval. Thépaut *et al.* (1993b) noticed a qualitative agreement between the two. Since then more evidence that analysis errors do project in practice on the unstable manifold has been shown experimentally by Rabier *et al.* (1996) and theoretically by Pires *et al.* (1995). In order to quantify the results of Thépaut *et al.* (1993b), we evaluate the projection of the analysis increments produced by 4D-Var on the most unstable subspace.

Following Lorenz (1965) (see also Buizza *et al.* 1993 for the practical aspects), we compute the so-called optimal modes which are the directions in the phase space E of fastest energy growth over the considered time interval: the 24-hour assimilation window. The

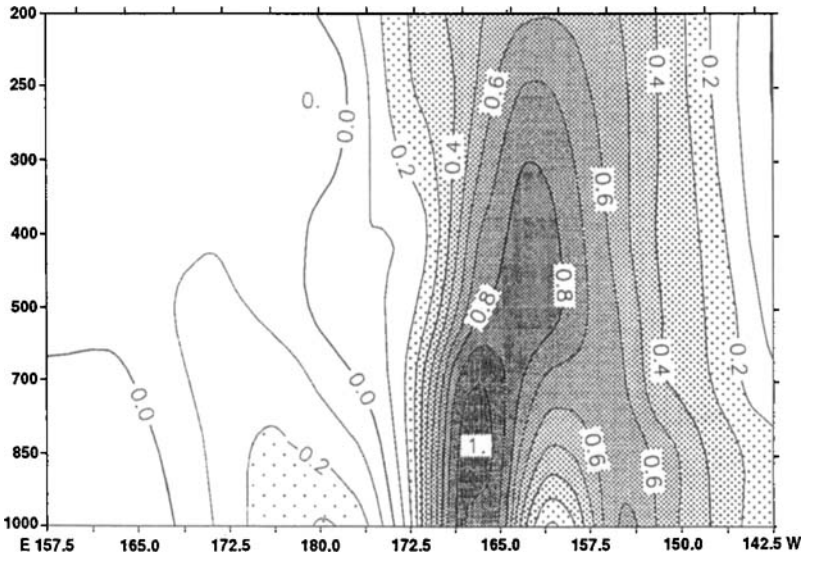

Figure 12. Cross-section of the 4D-Var structure function, obtained with an observation at location (42°N, 168.75°W, 1000 hPa). Contour interval: 0.1 m.

local area over which the error growth is maximized is $\Sigma = (25°\text{N}/85°\text{N}–120°\text{E}/120°\text{W})$ which includes our area of interest.

In mathematical terms, we seek perturbations $v(t_0)$ of unity energy norm at time t_0 which maximize, at time t_n, the energy of $\mathbf{TM}'v(t_0)$ where $\mathbf{M}'$ is the tangent linear model and $\mathbf{T}$ a local projection operator on the domain Σ. The energy norm is defined (Thépaut and Courtier 1991) as the quadratic invariant of the linearized primitive equations in the vicinity of an isothermal state of rest.

A classic algebraic result is that the $v(t_0)$ are the singular vectors of the operator $\mathbf{TM}'$ which in turn are the eigenvectors of $\mathbf{M}'^*\mathbf{T}^*\mathbf{TM}'$. The dominant eigenvectors may be computed in practice using an iterative Lanczos algorithm.

Let $\mathbf{v}_1, \mathbf{v}_2, \ldots, \mathbf{v}_N$ be the first N dominant singular vectors transported at time t_n by the tangent linear model and $\delta\mathbf{x} = \mathbf{x}^a(t_n) - \mathbf{x}^b(t_n)$ be the analysis increment produced by 4D-Var at the end of the assimilation period. $\delta\mathbf{x}$ may be decomposed as

$$\delta\mathbf{x} = \lambda_1.\mathbf{v}_1 + \ldots + \lambda_N.\mathbf{v}_N + \mathbf{r} \tag{14}$$

where $\mathbf{r}$ is the residual, orthogonal to the most unstable subpace spanned by the set $(\mathbf{v}_1, \mathbf{v}_2, \ldots, \mathbf{v}_n)$. The vectors $\mathbf{v}_i$ being orthogonal, λ_i is given by

$$\lambda_i = \frac{\langle \delta\mathbf{x} | \mathbf{v}_i \rangle}{\|\mathbf{v}_i\|^2} \tag{15}$$

where $\langle . | . \rangle$ denotes the energy norm.

The percentage p_i of explained variance of $\delta\mathbf{x}$ by the vector $\mathbf{v}_i$ is

$$p_i = \lambda_i^2 . \frac{\|\mathbf{v}_i\|^2}{\|\delta\mathbf{x}\|^2} = \frac{(\langle \delta\mathbf{x} | \mathbf{v}_i \rangle)^2}{\|\mathbf{v}_i\|^2 . \|\delta\mathbf{x}\|^2} \tag{16}$$

For reasons of computational cost, only a limited number (30) of iterations of the Lanczos algorithm were performed and 13 singular vectors could be computed with satis-

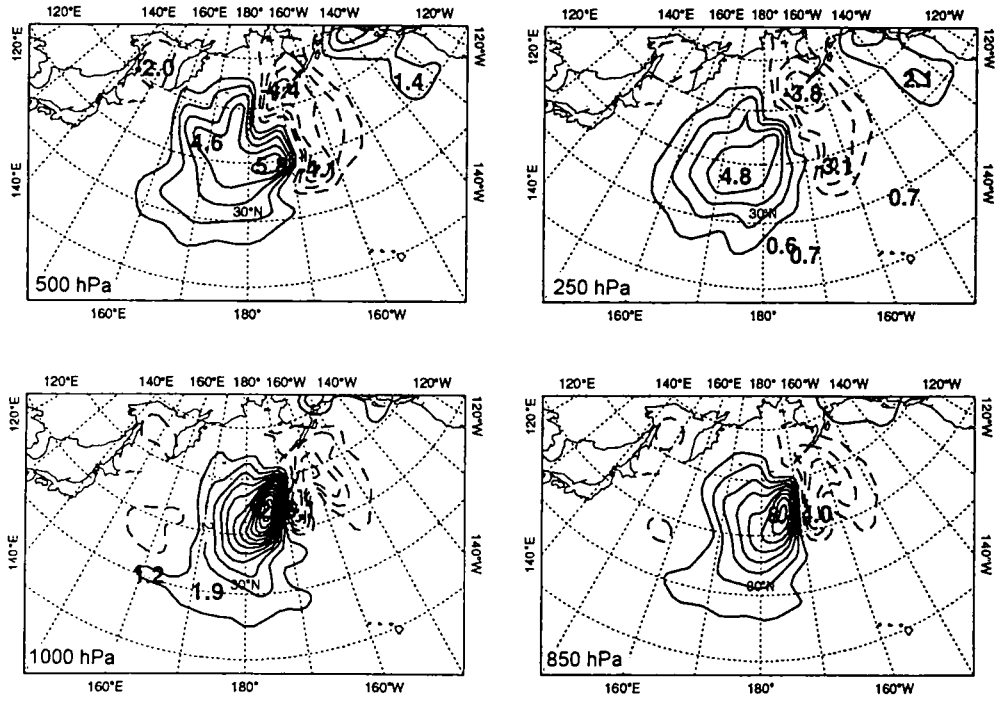

Figure 13. Same as Fig. 7 but for a single height observation at 1000 hPa at the location (42°N, 180°W). Contour interval: 0.1 m.

factory accuracy. The horizontal and vertical resolution of the singular vectors computation is the same as the 4D-Var experiments, T63L19.

The signature of the dominant singular vectors evolved at final time is concentrated close to the surface in the vicinity of the low but also with some significant features at the jet level. We have focused on the observation at 1000 hPa located in the same area leading to the analysis increments which are displayed in Fig. 13.

Following (16), the variance of these analysis increments explained by the first 13 eigenvectors is 29%. More interesting is that almost 21% comes from only one singular vector (the third one). Fig. 14 presents the stream function field of this singular vector at final time, as it evolved in the tangent-linear model; it is plotted for the four model levels closest to 1000, 850, 500 and 250 hPa. When comparing Fig. 13 and Fig. 14, one notices strong similarities at the surface and 850 hPa (especially the two fronts extending south at 170°W and 155°W). Although the observation is located at 1000 hPa, the 250 hPa increments also show three distinct patterns orientated south-west north-east which match the structure of the singular vector at the same level.

Although 4D-Var can use the observations to improve the analysis along the most unstable manifold, the analysis uncertainty will nevertheless remain maximal along these directions since it corresponds to directions where past observations are least informative (Pires *et al.* 1995). The suggestion that the dynamical part of the analysis error covariances at the end of the assimilation period can be described to a reasonable accuracy by a limited number of singular vectors computed over the same time period is of utmost importance for the cycling of 4D-Var, allowing the practical implementation of a simplified Kalman filter (Courtier 1993).

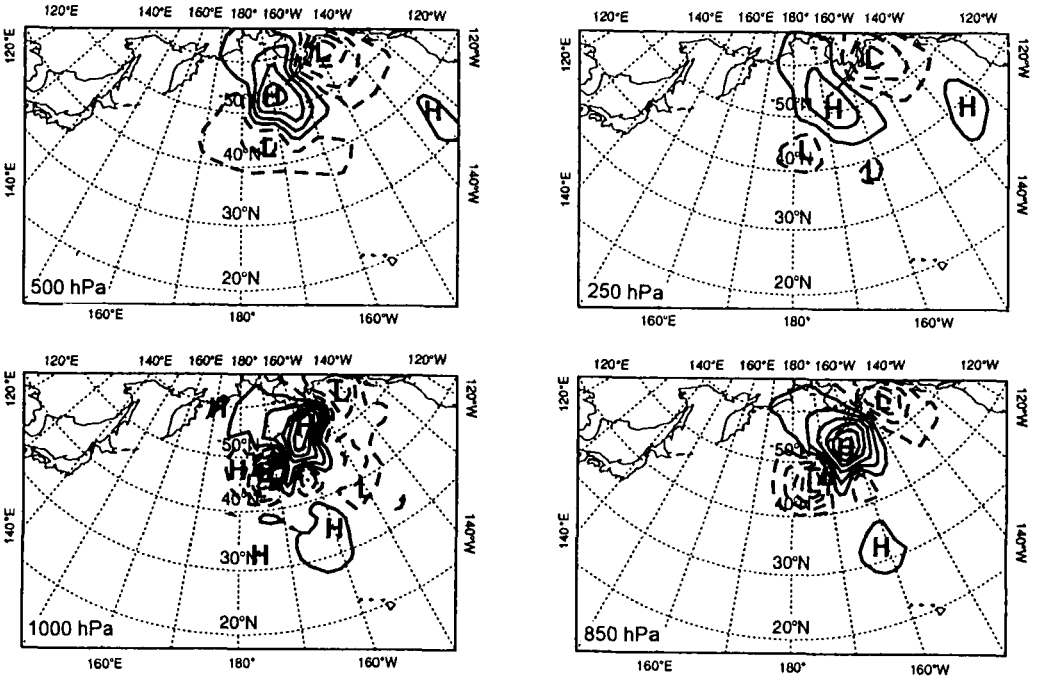

Figure 14. Third evolved eigenvector, represented here in terms of stream function for model levels closest to the 1000, 850, 500 and 250 hPa levels. Contour interval : 2×10^4 m^2 s^{-1}.

(*b*) *Spectral aspects*

Figures 15–17 display the logarithm of the power spectrum at total wave number m of geopotential increments at 1000 , 500 and 250 hPa respectively, produced by 4D-Var with a single height observation also located at respectively 1000, 500 and 250 hPa and for three different geographical areas (represented by the dashed, dotted and dot-dashed curves). The thick curve corresponds to the geopotential increment produced by 3D-Var with the same observation.

At 1000 hPa in high pressure areas (Fig. 15 dashed and dot-dashed curves), the large-scale amplitude of the increments is larger for 4D-Var than for 3D-Var. The slope is similar and the maxima are similarly located at around wave number 10. For an observation located close to the depression (dotted curves), the amplitude is smaller for the large scales and the peak is shifted towards wave number 15. As for the inertial range, the slope is similar for all the 4D-Var points, the 3D-Var slope being much steeper. The increments produced at 1000 hPa are then more energetic than the 3D-Var ones, especially for the small scales.

At 500 and 250 hPa (Fig. 16 and Fig. 17), the amplitude of the large-scale 4D-Var increments is bigger than that of the 3D-Var ones, even at the trough location; the peak wave number becomes smaller, reaching 7 for the 3 points at the jet level. The difference of slope between 3D and 4D-Var gradually becomes smaller from 1000 hPa to 250 hPa.

The average slopes in the inertial range of 4D and 3D-Var increments are summarized in Table 2.

The fact that the amplitude of the 4D-Var increments is generally larger and that there is more energy in the small scales in 4D-Var than in 3D-Var, is consistent with the horizontal increment maps (Fig. 5, Fig. 6, Fig. 7 and Fig. 13), where one notices that 4D-Var increments are higher than the 3D-Var ones, with more detailed small structures and spread over a larger area.

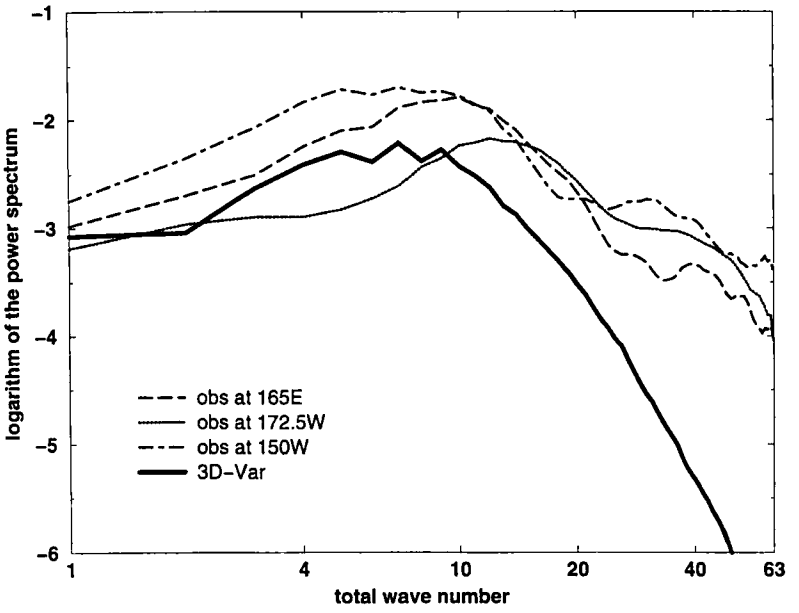

Figure 15. 4D-Var increments power spectra at 1000 hPa produced by single observations located between longitude 165°E and 150°W at the same level. And for reference: 3D-Var increments spectrum for one observation also located at 1000 hPa.

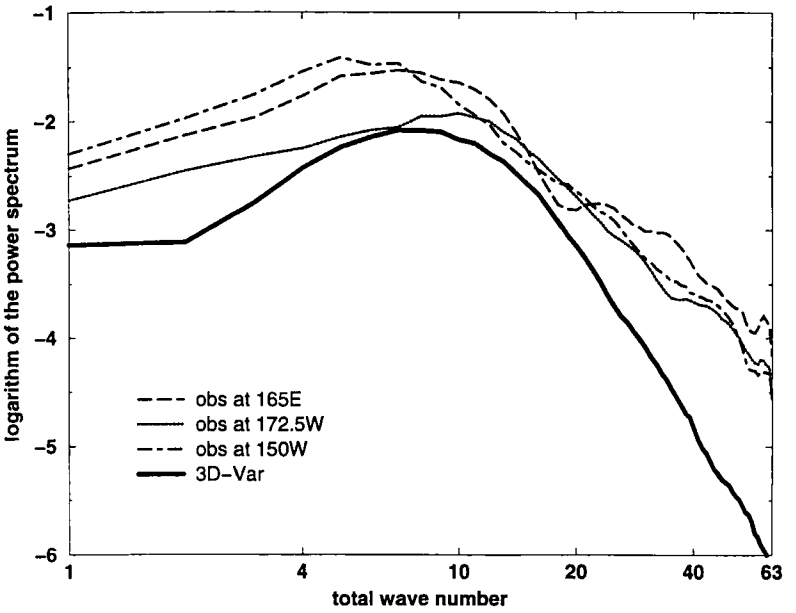

Figure 16. 4D-Var increments power spectra at 500 hPa produced by single observations located between longitude 165°E and 150°W at the same level. And for reference: 3D-Var increments spectrum for one observation also located at 500 hPa.

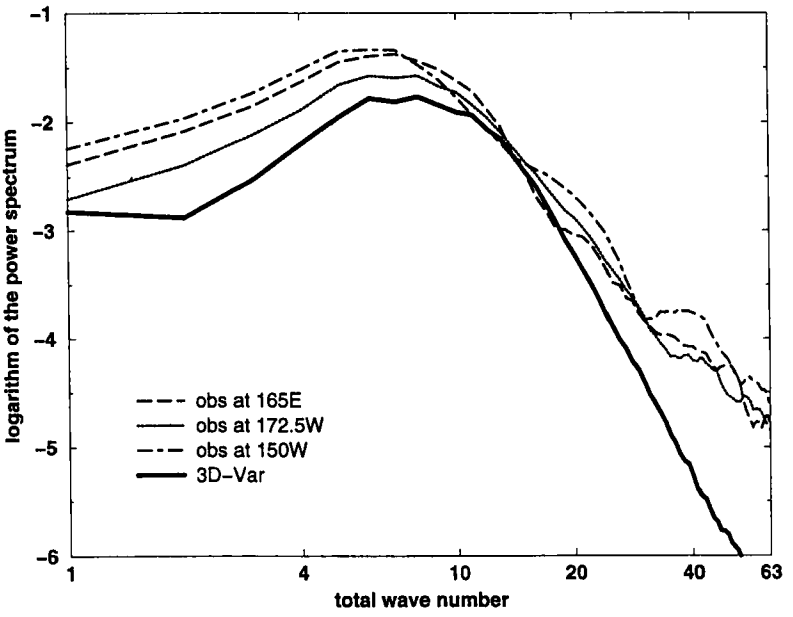

Figure 17. 4D-Var increments power spectra at 250 hPa produced by single observations located between longitude 165°E and 150°W at the same level. And for reference: 3D-Var increments spectrum for one observation also located at 250 hPa.

TABLE 2. SLOPE OF THE 3D AND 4D-VAR INCREMENTS SPECTRUM IN THE INERTIAL RANGE

height (hPa)	3D-Var slope	4D-Var average slope
1000	5.7	2.9
500	6.1	3.3
250	7.0	3.3

(c) *Impact of the temporal dimension*

The impact of the temporal dimension on the spatial structure of the analysis increments has also been studied. Two additional sets of similar experiments have been performed in the context of a 4D-Var assimilation over 12 hours (from 5 March 0000 UTC) and over 6 hours (from 5 March 0600 UTC).

Over short time periods, the growth rate of the most unstable modes remains small. The consequence is that in the background error covariance matrix $\mathbf{M}'\mathbf{B}(t_0)\mathbf{M}'^{\mathrm{T}}$ which spreads the analysis increments, the matrix $\mathbf{B}(t_0)$ becomes dominant. This can be seen on Figs. 18 (a) and (b) which represent the analysis increments produced by one height observation located at 1000 hPa (42°N 157.5°E) in the context of a 12-hour and 6-hour 4D-Var respectively, and which can be compared to Fig. 13.

When 4D-Var is performed over 12 hours, one can still see the dynamical signal of the analysis increments at 1000 and 850 hPa, but it is much less intense than on Fig. 13. As for the 6-hour 4D-Var, the analysis increments are weakly distorted at the surface and remain close to isotropy and barotropicity up in the atmosphere, although one may notice the presence of negative increments at 500 and 250 hPa.

Figures 19 (a) and (b) show the cross-section of the implied background error standard deviations obtained from the 12-hour 4D-Var and 6-hour 4D-Var respectively. Although

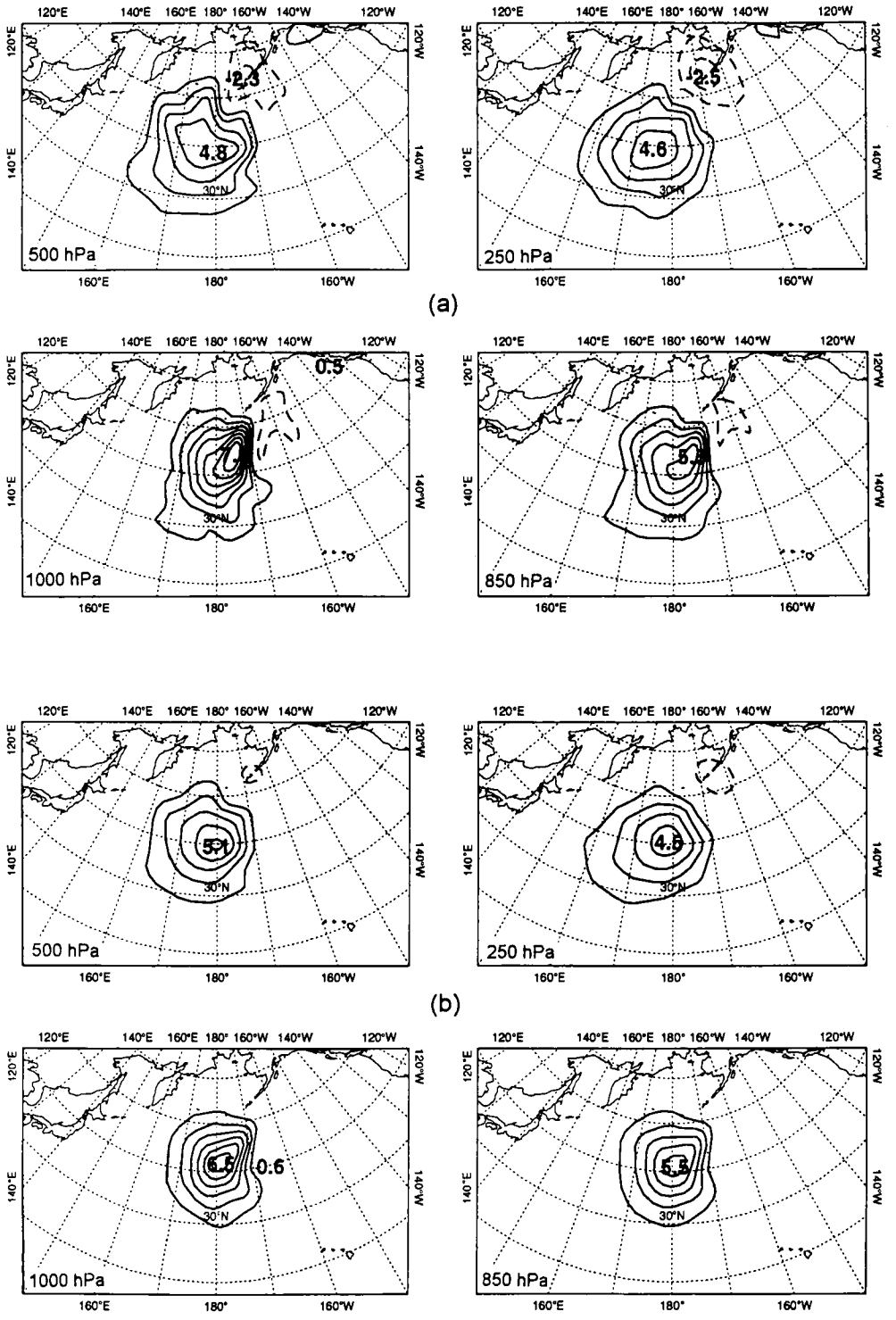

Figure 18. (a) Same as Fig. 13 but for 4D-Var performed over 12 hours. (b) Same as (a) but for a 4D-Var performed over 6 hours. Contour interval: 0.1 m.

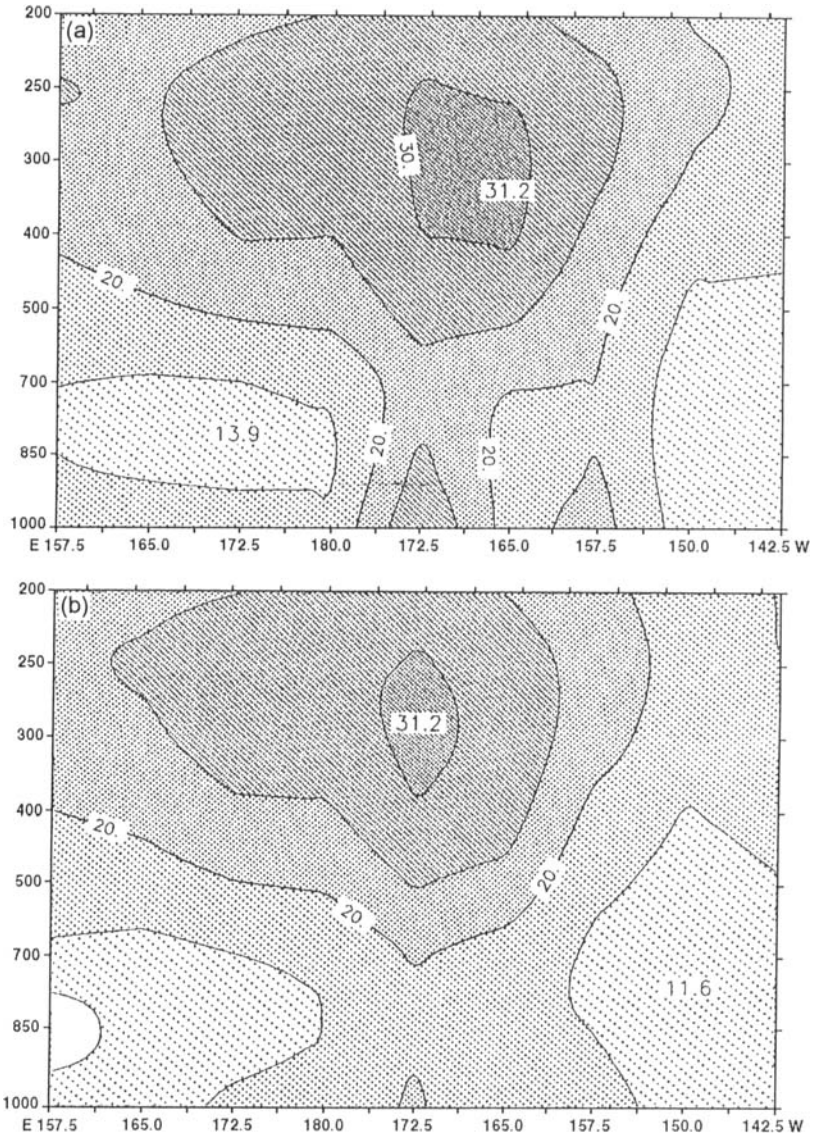

Figure 19. Cross-sections of background error standard deviations in 4D-Var. (a) 4D-Var 12 hours. (b) 4D-Var 6 hours. Contour interval: 5 m.

the shape of the σ_b fields presents some similarities with Fig. 10 (a), (i.e. maxima in the perturbed areas), the fields are nonetheless smoother and the extrema are generally lower.

In the case of the 6-hour 4D-Var, the implied σ_bs can be twice as low as what they are when 4D-Var is performed over 24 hours (see the location 42°N, 157.5°E, 1000 hPa in the anticyclonic area). They are even smaller than the ones specified in 3D-Var. A possible explanation lies in some inconsistencies between the isotropic structure functions specified at the beginning of the assimilation period and the dynamics, which lead to transients in some phase space directions implying such a reduction.

These results suggest that the length of the 4D-Var assimilation period is crucial to ensure fully developed dynamical structure functions. However, and regardless of the computing time considerations, the optimal time window in 4D-Var is also constrained by

the implicit assumption that the model is perfect and by the validity of the tangent linear hypothesis.

6. Concluding remarks

This paper describes several 4D-Var data assimilation experiments, which explore the flow dependency of the structure functions, implicit in the scheme. By making a series of single observation experiments, we have been able to exhibit these implied structure functions and the implied background error standard deviations in a baroclinic situation.

4D-Var produces much more complex increments than 3D-Var, especially in the vicinity of the low, where one notices a large sensitivity of the structure functions to the observation location. Differences between 4D-Var and 3D-Var are noticeable but to a lesser extent in anticyclonic areas.

The meridional extension of the study at 1000 hPa has shown a strong connection between maxima of background error standard deviations and areas of strong pressure gradient. This gives an insight on the potential weaknesses of the current 3D-Var system where the background error standard deviations are static. A strong link between the 4D-Var increments and the singular vectors of the tangent linear dynamics computed over the same time interval has been shown. This connection suggests the use of this information firstly to improve the conditioning of the minimization problem and secondly to estimate the analysis error covariance matrix needed to cycle 4D-Var properly (Courtier 1993; Fisher and Courtier 1995).

Our study of the time dimension shows that the assimilation period has to be long enough to ensure fully developed dynamical structure functions.

4D-Var produces structure functions significantly different from the static ones used in 3D-Var; are they right? Several features, in particular their baroclinicity, can be considered as an improvement. The quality of the structure functions implicitly used in 4D-Var depends on four elements. First, the structure functions specified at initial time are, in this study, the static ones used in 3D-Var. Given that a forecast is sensitive to the initial conditions, it is likely that the initial structure functions are an important element in the prediction of the forecast error covariance matrix. Second, the implicit closure of the scheme (in the turbulence vocabulary) is of zero order here and relies critically on the accuracy of the tangent linear hypothesis for describing the short-range forecast errors. This difficulty has, to the best of our knowledge, not yet been encountered in 4D-Var assimilation with real observations, but the small scale pattern of the implied structure functions seen during this study seems to indicate a potential problem. Third, 4D-Var relies on the perfect model assumption. This weakness may be relaxed using a weak formulation and algorithm relying on e.g. the representer technique (Bennett *et al.* 1993). However as the current knowledge on the model error term of the second order moment equation of the Kalman filter is very limited, documenting the statistical properties of the model errors is a scientific challenge for data assimilation (Dee 1995). And last, the accuracy of the structure functions depends on the accuracy of the model itself. The experiments presented here have been done with a quasi-adiabatic model at a resolution of T63. In the depression, latent heat release was missing and we do not know the magnitude of the impact of the missing physical parameterizations.

As surface friction with a constant surface roughness was included in the model, it was possible to assess the impact of the surface roughness on the implied structure functions. It turned out that a variation of the surface roughness can produce significant effects on the effective standard deviations. A coefficient corresponding (through the Charnock formula) to a wind of 15 m s^{-1} gives a σ_b of 36 m at location (42°N, 171°W, 1000 hPa). A coefficient

corresponding to 25 m s^{-1} produces a value of 32 m, which corresponds to a variation of 12% compared to the previous one.

The large sensitivity of the structure functions to a small change in the model suggests that the better the trajectory (in the vicinity of which the adjoint model is linearized) and the better the adjoint model, the more realistic the structure functions.

The incremental formulation of 4D-Var, which is described in Courtier *et al.* (1994) consists of solving an approximate quadratic problem with a model linearized in the vicinity of a trajectory that is as accurate as possible. The scheme allows for a gradual improvement in the linearized model, for example by introducing some physical parametrizations progressively.

It is hoped that this framework will lead to more realistic structure functions and that the potential decribed here for using flow dependent analysis error covariances will be fully exploited in 4D-Var.

Acknowledgements

The collaboration and the support of the ECMWF Research Department Data Division is gratefully acknowledged. We would like to thank A.Hollingsworth for his comments. Carole Edis carefully checked the manuscript.

The minimization algorithm was provided by Institut National de Recherche en Informatique et en Automatique (INRIA, France). The work was partially supported by the Groupement de Recherche 'Méthodes Variationnelles en Météorologie et Océanographie' funded by the Centre National de la Recherche Scientifique and by Météo France.

The last two authors were performing a research stage during their scholarship at Ecole Polytechnique, Paris, France, Robert Sadourny being their Professor.

References

Andersson, E., Pailleux, J., Thépaut, J.-N., Eyre, J., Kelly, G., Courtier, P. 1994 Use of cloud cleared radiances in 3D/4D variational data assimilation. *Q. J. R. Meteorol. Soc.*, **120,** 627–654

Bennett A. F., Leslie, L. M., Hagelberg, C. R., and Powers, P. E. 1993 Tropical cyclone prediction using a barotropic model initialized by a generalized inverse method. *Mon. Weather Rev.*, **121,** 1714–1729

Buizza, R., Tribbia, J., Molteni, F. and Palmer, T. 1993 Computation of optimal unstable structures for a numerical weather prediction model. *Tellus*, **45A,** 388–407

Cohn, S. E. and Parrish, D. F. 1991 The behaviour of the forecast error covariances for a Kalman filter in two dimensions. *Mon. Weather Rev.*, **119,** 1757–1785

Courtier, P. and Talagrand, O. 1987 Variational assimilation of meteorological observations with the adjoint vorticity equation. Part II. Numerical results. *Q. J. R. Meteorol. Soc.*, **113,** 1329–1368

1990 Variational assimilation of meteorological observations with the direct and adjoint shallow-water equations. *Tellus*, **42A,** 531–549

Courtier, P., Freydier, C., Geleyn, J. F., Rabier, F. and Rochas, M. 1991 The Arpege project at Météo-France: *Proc. of the 1991 ECMWF seminar on Numerical Methods in Atmospheric Models.* (Available from ECMWF)

Courtier, P., Andersson, E., Heckley, W., Kelly, G., Pailleux, J., Rabier, F., Thépaut, J.-N., Undén, P., Vasiljevic, D., Cardinali, C., Eyre, J., Hamrud, M., Haseler, J., Hollingsworth, A., McNally, A. and Stoffelen, A. 1993 *ECMWF Res. Dep. Technical Memorandum*, **No 194**

Courtier, P.	1993	Introduction to numerical weather prediction data assimilation methods. Pp. 189–207 in *Proc. of the 1993 ECMWF seminar on Developments in the Use of Satellite Data in Numerical Weather Prediction.* (Available from ECMWF)
Courtier, P., Thépaut, J.-N. and Hollingsworth, A.	1994	A strategy for operational implementation of 4D-Var, using an incremental approach. *Q. J. R. Meteorol. Soc.*, **120,** 1367–1388
Daley, R.	1991	*Atmospheric Data Analysis.* Cambridge University Press, 457pp
Dee, D.	1995	Testing the perfect model assumption in variational data assimilation. Pp. 49–54 in *Proc. of the Second International Symposium on Assimilation of Observations in Meteorology and Oceanography.* WMO/TD No 651, Tokyo, Japan, 13–17 March 1995
Derber, J. C.	1987	Variational four-dimensional analysis using quasi-geostrophic contraints. *Mon. Weather Rev.*, **115,** 998–1008
Fisher, M. and Courtier, P.	1995	Three Algorithms for Estimating the Covariance Matrix of Analysis Error in Incremental Variational Data Assimilation. Pp. 229–234 in *Proc. of the Second International Symposium on Assimilation of Observations in Meteorology and Oceanography.*, WMO/TD No 651, Tokyo, Japan, 13–17 March 1995
Gauthier, P., Courtier, P. and Moll, P.	1993	Assimilation of Simulated Wind Lidar Data with a Kalman Filter. *Mon. Weather Rev.*, **121,** 1803–1820
Ghil, M., Cohn, S., Tvantzis, J., Bube, K. and Isaacson, E.	1980	Application of estimation theory to numerical weather prediction. Pp. 249–334 in *1980 ECMWF seminar on 'Data assimilation methods'.* Also in *Dynamic Meteorology, Data assimilation methods.* (Eds. L. Bengtsson, M. Ghil, E. Kallen), Springer-Verlag 1981
Ghil, M. and Malanotte-Rizzoli, P.	1991	Data assimilation in meteorology and oceanography. *Adv. Geophys.*, **33,** 141–266
Gilbert, J. Ch. and Lemaréchal, C.	1989	Some numerical experiments with variable storage quasi-Newton algorithms. *Mathematical Programming*, **B25,** 407–435
Ide, K., Bennett, A. F., Courtier, P., Ghil, M., Lorenc, A. C.	1995	Unified notation for Data Assimilation: Operational, Sequential and Variational. *J. Met. Soc. Japan*, submitted
Jazwinski, A. H.	1970	*Stochastic Processes and Filtering Theory.* Academic Press, New York
Le Dimet, F. X. and Talagrand, O.	1986	Variational algorithms for analysis and assimilation of meteorological observations: theoretical aspects. *Tellus*, **38A,** 97–100
Lönnberg, P. and Hollingsworth, A.	1986	The statistical structure of short range forecast errors as determined from radiosonde data. PartII: The covariance of height and wind errors. *Tellus*, **38A,** 137–161
Lorenc, A. C.	1986	Analysis methods for numerical weather prediction. *Q. J. R. Meteorol. Soc.*, **112,** 1177–1194
Lorenz, E. N.	1965	A study of the predictability of a 28-variable atmospheric model. *Tellus*, **17,** 321–333
Navon, I. M., Zou, X., Derber, J. and Sela, J.	1992	Variational data assimilation with with an adiabatic version of the NMC spectral model. Mon. Weather Rev., **120,** 1747–1766
Parrish, D. P. and Derber, J. C.	1992	The National Meteorological Center's spectral statistical-interpolation analysis system. *Mon. Weather Rev.*, **118,** 1747–1763
Phillips, N. A.	1986	The spatial statistics of random geostrophic modes and first-guess errors. *Tellus*, **38A,** 314–332
Pires, C., Vautard, R. and Talagrand, O.	1996	On extending the limits of variational assimilation in nonlinear chaotic systems. *Tellus*, **48A** (in press)
Rabier, F. and Courtier, P.	1992	Four-dimensional assimilation in the presence of baroclinic instability. *Q. J. R. Meteorol. Soc.*, **118,** 649–672
Rabier, F. and McNally, A.	1993	Evaluation of Forecast Error Covariance Matrix. *ECMWF Res. Dep. Technical Memorandum*, **No 195**
Rabier, F., Klinker, E., Courtier, P. and Hollingsworth, A.	1996	Sensitivity of forecast errors to initial conditions. *Q. J. R. Meteorol. Soc.* **121,** 121–150
Shaw D., Lönnberg, P., Hollingsworth, A. and Unden, P.	1987	Data assimilation: The 1984/85 revisions of the ECMWF mass and wind analysis. *Q. J. R. Meteorol. Soc.*, **113,** 533–566
Simmons, A. J. and Hoskins, B. J.	1978	The life cycles of some nonlinear baroclinic wawes. *J. Atmos. Sci.*, **35,** 414–432

Talagrand, O. and Courtier, P. 1987 Variational assimilation of meteorological observations with the adjoint vorticity equation. Part 1: Theory. *Q. J. R. Meteorol. Soc.*, **115,** 1311–1328

Thépaut, J.-N. and Courtier, P. 1991 Four-dimensional variational data assimilation using the adjoint of a multilevel primitive-equation model. *Q. J. R. Meteorol. Soc.*, **117,** 1225–1254

Thépaut, J.-N., Vasiljevic, D., Courtier, P. and Pailleux, J. 1993a Variational assimilation of conventional meteorological observations with a multilevel primitive equation model. *Q. J. R. Meteorol. Soc.*, **119,** 153–186

Thépaut, J.-N., Hoffman, R. and Courtier, P. 1993b Interaction of dynamics and observations in a four dimensional variational assimilation. *Mon. Weather Rev.*, **121,** 3393–3413

Undén, P. 1989 Tropical data assimilation and analysis of divergence. *Mon. Weather Rev.*, **117,** 2495–2517